Rare Met. (2023) 42(10):3430–3442
https://doi.org/10.1007/s12598-023-02440-8

RARE METALS

ORIGINAL ARTICLE

Tailoring mechanical heterogeneity, nanoscale creep deformation and optical properties of nanostructured Zr-based metallic glass

Jing-Xian Cui, Qiang Luo*, Zheng-Guo Zhang, Jing-Tao Zhu*, Bao-Long Shen*

Received: 16 April 2023 / Revised: 31 May 2023 / Accepted: 1 June 2023 / Published online: 4 September 2023

Abstract Metallic glasses are spatially heterogeneous at the nanometer scale. However, the effects of external excitation on their structural and mechanical heterogeneity and the correlation to their properties are still unresolved. Nanoindentation, atomic force microscopy (AFM) and high-resolution transmission electron microscopy (HRTEM) were carried out to explore the effects of cryogenic thermal cycling (CTC) on mechanical/structural heterogeneity, nanoscale creep deformation and optical properties of nanostructured metallic glass thin films (MGTFs). The results indicate that CTC treatment alters the distribution fluctuations of hardness/modulus and energy dissipation and results in an increase-then-decrease variation in mechanical heterogeneity. By applying Maxwell–Voigt model, it can be shown that CTC treatment results in a remarkable activation of more defects with longer relaxation time in soft regions but has only a slight effect on defects in hard regions. In addition, CTC treatment increases the transition time from primary-state stage to steady-state stage during creep deformation. The enhanced optical reflectivity of the MGTFs after 15 thermal cycles can be attributed to increased aggregation of Cu and Ni elements. The results of this study shed new light on understanding mechanical/structural heterogeneity and its influence on nanoscale creep deformation and optical characteristics of nanostructured MGTFs, and facilitate the design of high-performance nanostructured MGTFs.

Keywords Metallic glass thin films (MGTFs); Cryogenic thermal cycling (CTC); Structural heterogeneity; Mechanical and creep properties; Optical characteristics

1 Introduction

Bulk metallic glasses (BMGs) have emerged as promising structural and functional materials because of their excellent properties such as high yield strength, enhanced magnetic properties and catalytic activity [1–4]. However, their widespread application is precluded by their poor ductility and general tendency to fail catastrophically with low tensile plasticity under loading [5]. Their plasticity can be significantly improved by reducing their thickness to the micro or nanoscale owing to strong size effect [6, 7]. Accordingly, metallic glass thin films (MGTFs), which can overcome catastrophic shear stability and glass-forming ability (GFA) limitations, have recently received increasing attention due to their significant application prospects in micro-electro-mechanical system devices, commercial blades, mold forming, protective coatings, optical coatings, solar heaters and sensors [8, 9].

Recently, ultrastable glasses (SMGs) and nanostructured glasses (NGs), which are relatively new comers to metallic glass family, have been developed to exhibit considerably enhanced thermal stability, mechanical and magnetic properties, catalytic activity and biocompatibility [10–12]. SMGs were initially created by tuning substrate temperature (T_{sub}) within the optimal window of 0.75–0.85 T_g (T_g

J.-X. Cui, Q. Luo*, Z.-G. Zhang, B.-L. Shen*
School of Materials Science and Engineering, Jiangsu Key Laboratory for Advanced Metallic Materials, Southeast University, Nanjing 211189, China
e-mail: q.luo@seu.edu.cn

B.-L. Shen
e-mail: blshen@seu.edu.cn

J.-T. Zhu*
School of Physics Science and Engineering, Tongji University, Shanghai 200092, China
e-mail: jtzhu@tongji.edu.cn

is the glass transition temperature of ordinary glass) [13, 14]. Later, Luo et al. [13] reported that SMGs could also be created with T_{sub} far below T_g ($T_{sub} \approx 0.43\ T_g$) at a low deposition rate of 1 nm·min^{-1} in $Cu_{46}Zr_{46}Al_8$ films. Sun et al. [12] found that the critical deposition rate for SMGs formation was directly linked to the degree of structural heterogeneity. In $Zr_{50}Cu_{50}$, $Zr_{50}Cu_{44.5}Al_{5.5}$ and $Zr_{50}Cu_{41.5}Al_{5.5}Mo_3$ MGTFs, deposition rates of less than 8 nm·min^{-1} were required to yield more heterogeneous structure and lower energy state underlying their ultrastability. Luo et al. [15] reported that a high degree of structural and mechanical heterogeneity was important for SMGs formation. Compared to conventional MGTFs, nanostructured MGTFs fabricated by various methods [11, 16] have a unique structural heterogeneity (nanograin/nanoglobular interfaces and elemental segregation), which has a strong influence on their thermal stability and chemical/mechanical properties [12, 17, 18]. For example, Cu rich interfaces and Zr rich relaxed cores in $Zr_{50}Cu_{50}$ and $Cu_{64}Zr_{36}$ NGs lead to an increased crystallization temperature and improve their tensile strain, hardness and modulus [16, 18]. Ni–P NGs with a high-energy state and unique heterogeneous microstructure exhibit significantly enhanced water splitting catalytic performance [11]. Despite a number of investigations into SMGs and NGs (which mainly focused on the effects of composition and preparation conditions), the nature of structural/mechanical heterogeneity and its correlation with mechanical and physical properties of SMGs and NGs are still poorly understood.

In this study, nanostructured $Zr_{64.13}Cu_{15.75}Ni_{10.12}Al_{10}$ (at%) MGTFs were prepared by magnetron sputtering method at a low deposition rate of 3.97 nm·min^{-1}. The effects of cryogenic thermal cycling (CTC) treatment on structural/mechanical heterogeneity, nanoscale creep deformation and optical characteristics were investigated in detail. The results indicate that CTC treatment induces variations in spatial distributions of hardness/modulus and energy dissipation, which show an increase-then-decrease trend in mechanical heterogeneity. The evolution of activated flow defects during nanoscale creep deformation was determined through relaxation time spectrum based on Maxwell–Voigt model. The optical performances of MGTFs were enhanced by tuning their chemical heterogeneity and Cu and Ni segregation. The correlation between heterogeneous structure and their property changes during CTC is discussed.

2 Experimental

$Zr_{64.13}Cu_{15.75}Ni_{10.12}Al_{10}$ (at%) MGTFs with a thickness of 3 μm were prepared by magnetron sputtering using a multicomponent $Zr_{64.13}Cu_{15.75}Ni_{10.12}Al_{10}$ alloy as a target on cleaned Si (100) wafers. The deposition was conducted at a power of 100 W and deposition rate of 3.97 nm·min^{-1}. In each CTC cycle, MGTFs were firstly immersed in liquid nitrogen (77 K) for 1 min and then immediately immersed in hot silicone oil (333 K, polydimethylsiloxane) for 1 min, as shown schematically in Fig. 1a. MGTFs were subjected to CTC treatment for 5, 10, 15, 20 and 30 cycles. The as-deposited and CTC-treated samples are denoted as AD, CTC5, CTC10, CTC15, CTC20 and CTC30, respectively.

Nanoindentation tests were performed at room temperature using a NanoTest Vantage (Micro Materials Ltd.) with a standard Berkovich diamond indenter to study nanoscale creep deformation and spatial hardness (H) and modulus (E_r) distributions. The load and displacement resolutions were 3 nN and 0.001 nm, respectively. The nanoscale creep measurements were conducted according to the sequence shown in Fig. 1b. Experiments at constant loading rates of 0.1, 2.0 and 5.0 mN·s^{-1} were performed up to a load limit of 20 mN followed by a holding period of 100 s and subsequently unloading at the same loading rate. For spatial distributions of H and E_r, a distance of 30 μm between two neighboring indents and a maximum load of 10 mN was chosen to avoid interactions between nearby strained zones. At least five indentation tests were carried out under each condition to minimize the influence of noise. The results that deviated significantly from the other results were discarded. Thermal drift at any given time was negligible during the entire indentation creep experiment.

The phase shift and topography on a selected surface with dimensions of 250 nm × 250 nm were mapped using atomic force microscopy (AFM) (Multimode VIII, Bruker). The energy dissipation (E_{dis}) of the analyzed surface can be calculated from the phase-shift distributions as follows:

$$E_{dis} = \left[\frac{\pi K A_{sp} A_0}{Q}\sin\left(\frac{\pi}{2} - \varphi\right)\right] - \frac{A_{sp}}{A_0} \quad (1)$$

where A_{sp} and A_0 denote the set point and free amplitudes, respectively; φ is the phase shift; and K and Q are spring constant and damping factor, respectively. It should be mentioned that the tip-surface interaction was weak enough to avoid plastic deformation of the sample. Optical parameters such as refractive index (n), extinction coefficient (k) and reflectivity (R) were measured as a function of visible light wavelength (λ) using a reflection spectrometer (USPM-RU III, Olympus). The samples for high-resolution transmission electron microscopy (HRTEM) analysis were thinned using ion milling (Gatan Inc., PIPS-M691) under liquid nitrogen cooling conditions. The nanoscale elemental distributions were analyzed using energy-dispersive X-ray spectroscopy (EDS) in TEM. For high angle annular dark-field (HAADF) imaging, a probe semi-convergence angle of 10.5 mrad and collection semi-angle of 58–200 mrad were used.

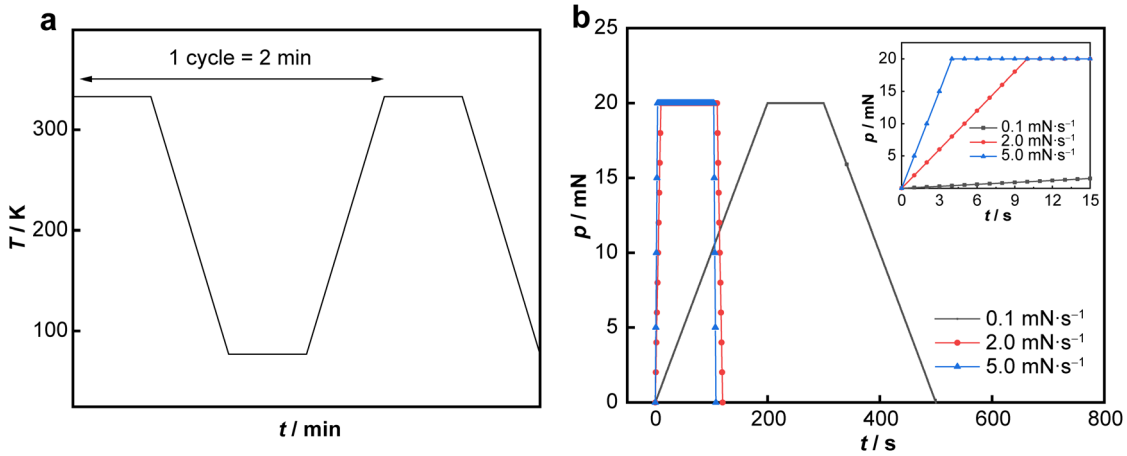

Fig. 1 **a** A schematic graph of CTC process; **b** load-time (p vs. t) plot for creep test of Zr-based MGTFs with different loading rates

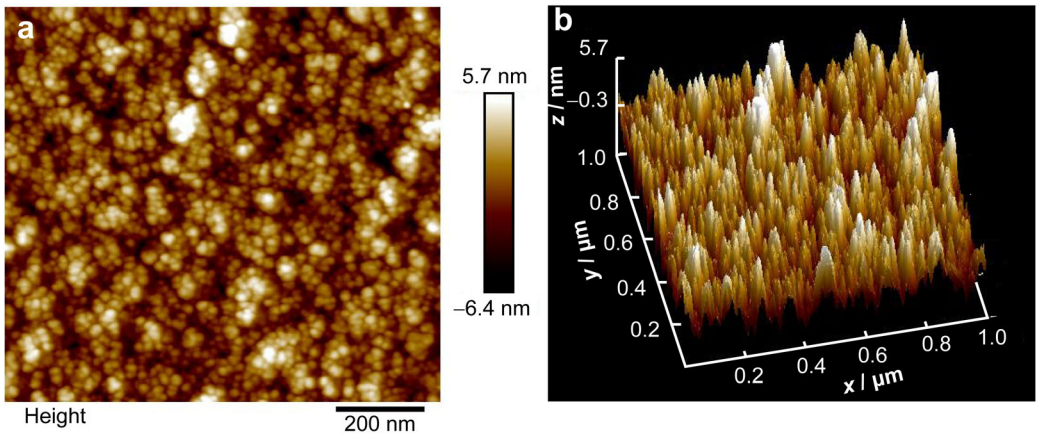

Fig. 2 **a** 2D and **b** 3D AFM images of Zr-based MGTFs

3 Results

3.1 Effects of CTC treatment on mechanical heterogeneity

Figure 2a, b shows two-dimensional (2D) and three-dimensional (3D) AFM images of AD Zr-based MGTFs. As shown in Fig. 2a, AD sample consists of nanometer-sized glassy regions and a hierarchical nanostructure due to the interplay between surface diffusivity and sputtering process [19]. From the topography results shown in Fig. 2b, the root-mean-square roughness (RMS) of AD sample was obtained as 1.53 nm, which was similar to that of reported Ni-Nb MGTFs which had an RMS of approximately 1.0–1.5 nm [5]. Nanoindentation tests were conducted to explore the influence of CTC cycles on nanoscale mechanical heterogeneity. The indentation depths are all below 300 nm, which is less than 10% of the film thickness. The possible influence of the substrate is therefore avoided. Figure 3a shows the load–displacement (P–h) curves of the samples before and after CTC treatment at a loading limit of 10 mN, where P is the loading force and h the instantaneous indenter displacement. None of the samples show a serration behaviour related to the formation and propagation of shear bands (SBs) [20]. The absence of significant serrated flow in MGTFs can be ascribed to their uniform plastic deformation [21]. Figure 3b shows the average hardness and modulus of the samples. The hardness is mainly distributed between 8.8 and 9.1 GPa and the modulus mainly between 122.0 and 125.7 GPa with little changes in their average values after CTC treatment.

The contour-line maps of nanoindentation hardness in a 10 μm × 10 μm square area shown in Fig. 4a–c clearly indicate different mechanical heterogeneities of the three samples. As shown in Fig. 4b, for sample CTC15, high-hardness areas are surrounded by continuous soft-hardness regions and form a relatively continuous grid structure. In addition, the degree of mechanical heterogeneity can be evaluated using the full width at half maximum (FWHM)

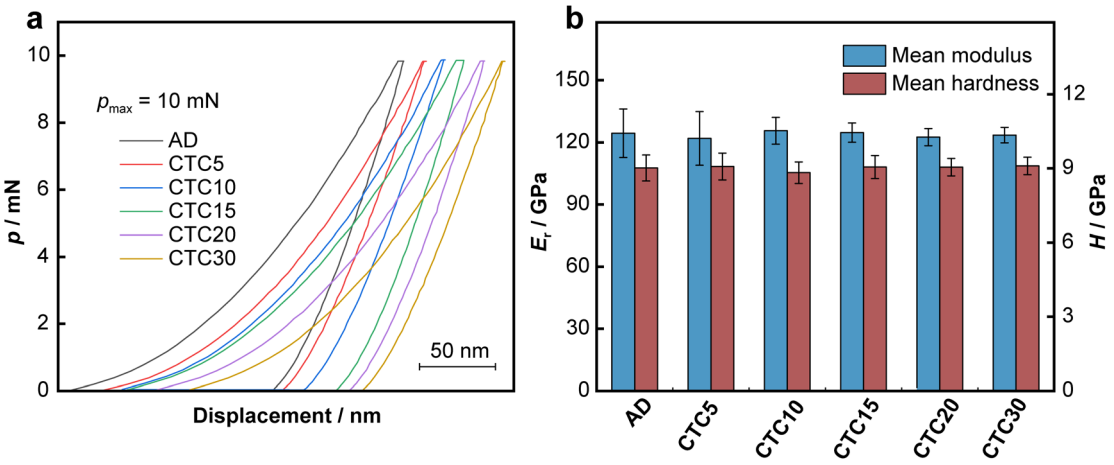

Fig. 3 **a** Load-depth (P–h) curves of samples before and after CTC treatment; **b** mean hardness (H) and modulus (E_r) as functions of CTC cycles at maximum load

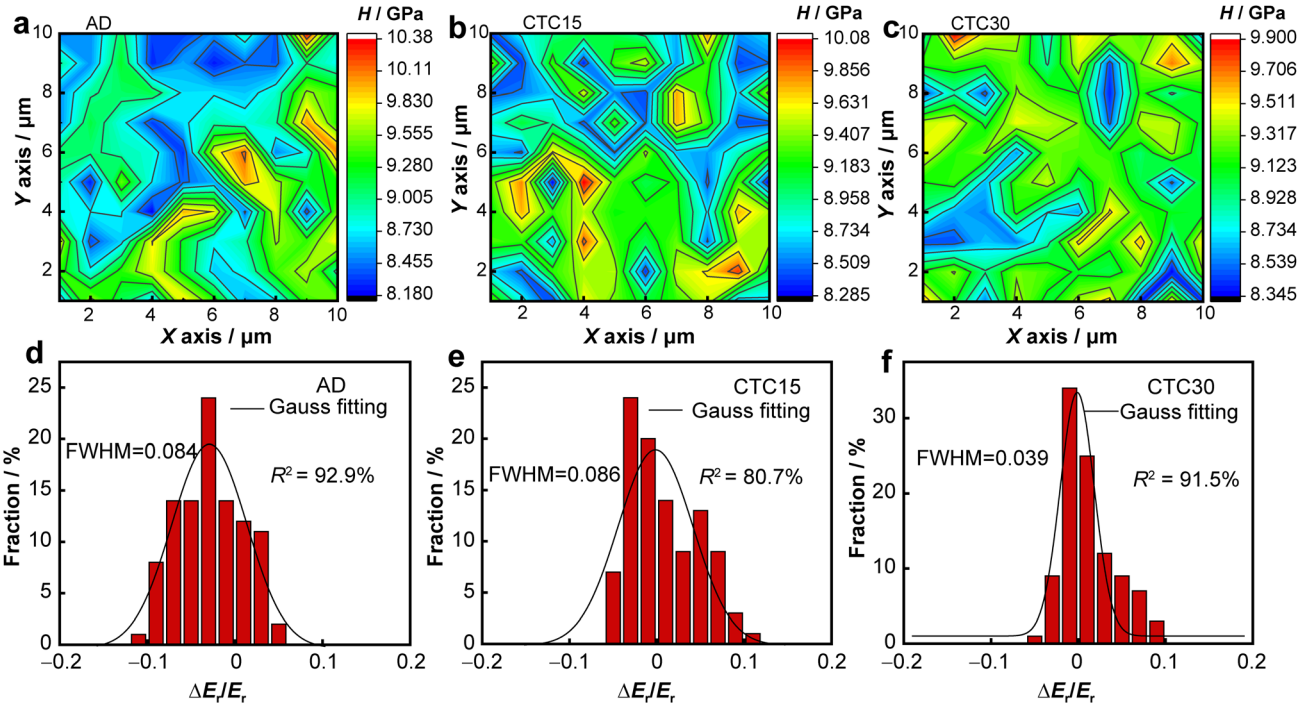

Fig. 4 Statistical data for H and E_r: **a–c** contour-line maps and **d–f** $\Delta E_r/E_r$ data of samples AD, CTC15, and CTC30

value of the modulus distribution curve. As shown in Fig. 4d–f, the statistical distributions of the modulus can also be fitted by Gaussian function. From the fitting, the FWHM of the relative modulus ($\Delta E_r/E_r$) of samples AD, CTC15, and CTC30 were determined to be 0.084, 0.086, and 0.039, respectively. That is, sample CTC15 exhibits a wider spatial distribution of modulus than the AD and CTC30 samples. This is likely due to the more heterogeneous structure and drastic activation of nanoscale soft zone regions in sample CTC15 [22]. These results indicate that the spatial distributions of the hardness and modulus are sensitive to the CTC cycles.

The mechanical heterogeneity at nanometer scale can be further characterized through local energy dissipation measurements using AFM. The interaction between AFM tip and the surface leads to energy dissipation in the glassy structure, which is manifested in viscoelastic response of MGTFs to dynamic forces [23]. The total energy stored is dependent on the extension of nanoscale viscoelastic fluctuations [24]. From Fig. 5a–c, it can be seen that there is an obvious change in energy dissipation distributions after

CTC treatment. The statistical distributions of energy dissipation can be fitted by a Gaussian distribution and scaled by corresponding FWHM. The FWHM of relative energy dissipation ($\Delta E/E$) is 0.36 for the sample AD, 0.39 for the sample CTC15, and 0.24 for the sample CTC30, as labelled in Fig. 5d–f. The broadened FWHM of $\Delta E/E$ in the CTC15 sample suggests an enhanced microstructural heterogeneity at the nanometer scale. It has been reported that apparent energy dissipation with fluctuating distributions is uncorrelated to surface roughness but originates from viscoelastic heterogeneity [25]. Specifically, densely packed and loosely packed regions exhibit low and high energy dissipation, respectively [23].

3.2 Nanoscale creep deformation

Indentation creep is always accompanied by competition between structural relaxation and elastic strain recovery and involves redistribution of free volume and rearrangement of atomic species [26]. Such structural evolution during creep deformation invariably causes activation and subsequent evolution of shear transition zones (STZs) in shearing events and therefore relates internal flow units to external mechanical properties [27, 28]. It is therefore important to investigate creep deformation in MGTFs to better understand potential mechanisms that influence the instantaneous plasticity. In addition, the creep deformation of nanostructured Zr-based MGTFs is reported for the first time.

As shown in Fig. 6a, creep displacement curve can be split into two stages comprising primary and steady-state stages. In the primary stage, creep displacement increases rapidly and the Kelvin units play a dominant role. In the steady-state stage, creep displacement tends to increase at a stable rate and the Maxwell dashpot plays an important role [29]. As the loading rate increases from 0.1 to 5.0 $mN{\cdot}s^{-1}$, the maximum creep displacement increases from 10.2 to 18.9 nm for the AD sample, from 11.8 to 22.1 nm for the CTC15 sample, and from 13.3 to 19.7 nm for the CTC30 sample. As shown in the inset of Fig. 6a, a typical fitted creep displacement curve obtained at the loading rate of 0.1 $mN{\cdot}s^{-1}$ can be fitted well using Maxwell–Voigt model that contains Maxwell and Kelvin units, where the correlation coefficient (R^2) is 96.2%. This model is applicable to creep deformation of viscoelastic materials during indentation. Herein, the creep displacement can be expressed as [21]:

$$h = h_0 + \sum_{i=1}^{n} h_i\left(1 - e^{-\frac{t}{\tau_i}}\right) + \frac{t}{\mu_0} \tag{2}$$

where t is holding time, h_i is indentation depth, τ_i is characteristic relaxation time of the i-th anelastic Kelvin unit, and μ_0 is viscoplastic constant of the Maxwell dashpot. Because MGs are structurally heterogeneous at nanoscale and contain liquid-like and solid-like regions [30, 31], two Kelvin units with Maxwell units were chosen

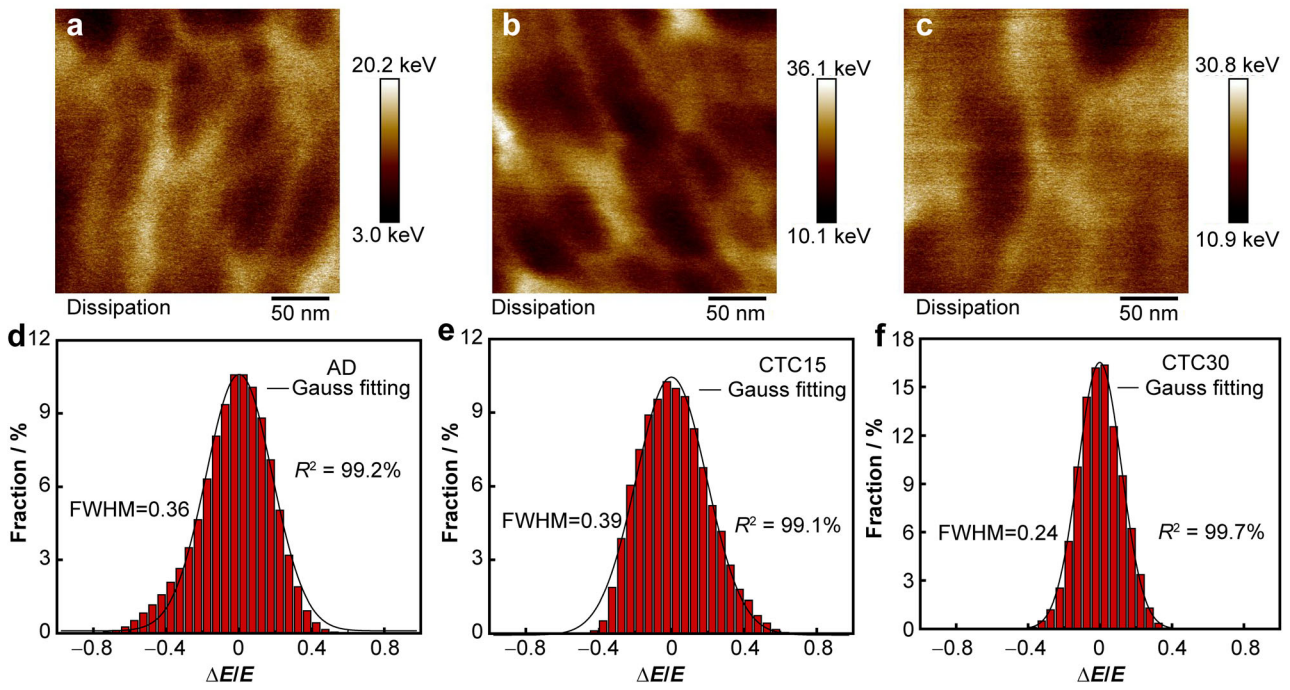

Fig. 5 **a–c** Energy dissipation images and **d–f** $\Delta E/E$ data of AD, CTC15 and CTC30 samples

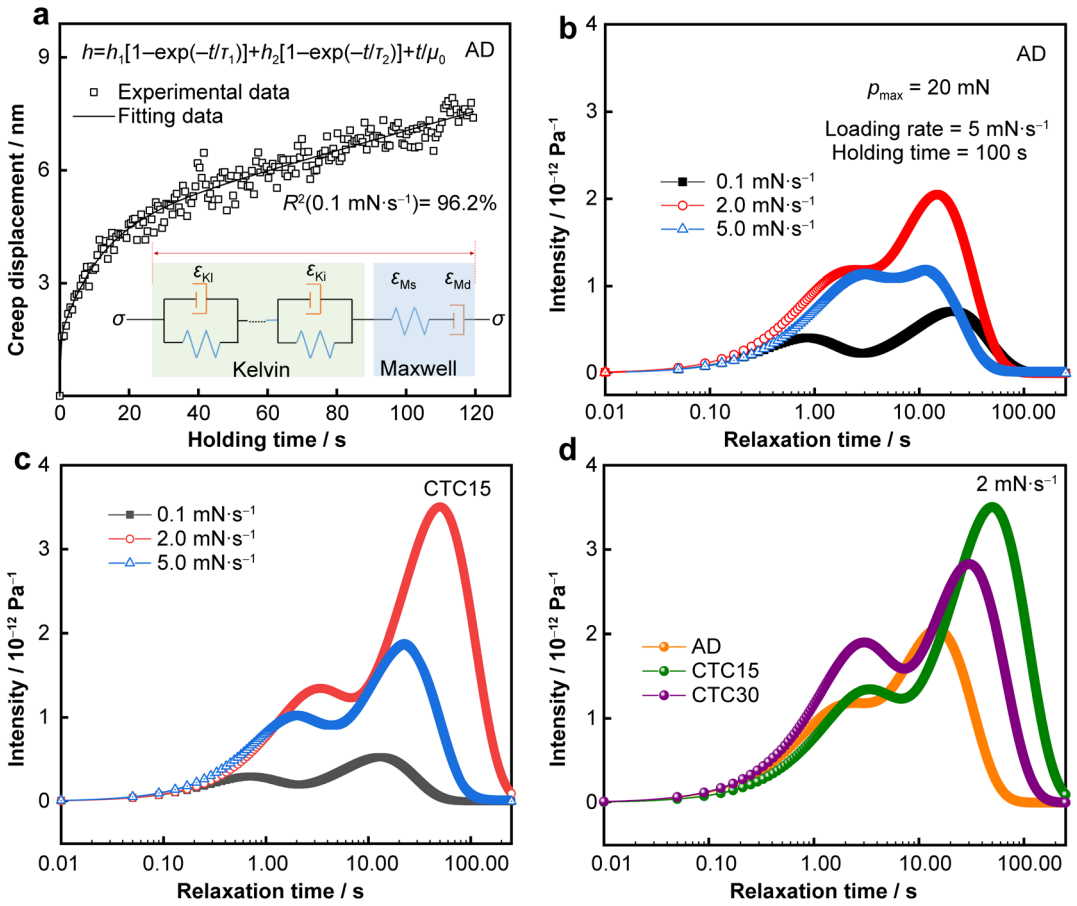

Fig. 6 **a** Typical fitting creep curve of AD sample at loading rate of 0.1 mN·s^{-1} and (inset) Maxwell–Voigt model used for analyzing creep curves; relaxation time spectra of samples **b** AD and **c** CTC15; **d** relaxation time spectra of samples AD, CTC15 and CTC30 under a loading rate of 2 mN·s^{-1}

to analyse creep displacement of the studied nanostructured MGTFs, that is, $n = 2$.

It has been shown that structural heterogeneity correlates well with two characteristic relaxation times τ_1 and τ_2 in Maxwell–Voigt model [4, 32]. The relaxation time spectrum obtained from Maxwell–Voigt model can accurately describe the two anelastic creep processes of MGTFs, which are expressed as [3]:

$$L(\tau) = \left[\sum_{i=1}^{n}\left(1+\frac{t}{\tau_i}\right)\frac{h_i}{\tau_i}e^{-\frac{t}{\tau_i}}\right]\frac{A_0}{P_0 h_{\text{in}}}t|_{t=2\tau} \quad (3)$$

where L is the spectrum intensity, A_0/P_0 is the inverse of hardness H, and h_{in} is the maximum indentation depth. Figure 6b, c shows the relaxation spectra of samples AD and CTC15 at different loading rates. As the loading rate increases from 0.1 to 5.0 mN·s^{-1}, both the peak intensities and relaxation time of the first and second peaks change notably. The intensity of relaxation spectra is reduced at a loading rate of 5 mN·s^{-1} in both AD and CTC-treated samples. This abnormal change in relaxation peaks may be due to the saturation of the activated defects at the loading rate of 2 mN·s^{-1} [3]. The comparison between relaxation spectra of AD and CTC-treated samples in Fig. 6d shows that there is a clear difference between the samples. A remarkable increase in the intensities of the two relaxation peaks is observed in CTC samples at a loading rate of 2 mN·s^{-1}, implying the activation of more defects in soft regions. The more pronounced intensity of the CTC15 secondary relaxation peak compared to that of sample CTC30 and the longer relaxation time τ_2 indicates the activation of more defects with larger sizes in soft regions. The intensity of the first relaxation peak increases with CTC cycles. The insignificant effect of CTC treatment on the relaxation time τ_1 indicates that there is only a small change in the size of the activated defects in hard regions.

The strain rate $\dot{\varepsilon}$ in nanoindentation creep tests can be estimated as [26]:

$$\dot{\varepsilon} = \frac{1}{h_i}\frac{\mathrm{d}h}{\mathrm{d}t} \quad (4)$$

where h_i is the instantaneous indenter displacement and $\mathrm{d}h/\mathrm{d}t$ is the creep rate fitted by Eq. (2). The stress σ can be calculated as [26]:

$$\sigma = \frac{P}{24.5h_i^2} \tag{5}$$

where P is the load applied to the sample. Figure 7a shows typical creep stress versus holding time curves of the AD sample under different loading rates. As the loading rate increases, creep stress decreases gradually except at 2 $mN{\cdot}s^{-1}$, which is consistent with the results of relaxation spectra shown in Fig. 6b. Figure 7b shows the creep stress curves as a function of the holding time at a loading rate of 5 $mN{\cdot}s^{-1}$. All the curves display the same tendency for reduced stress during the holding stage.

Figure 7c shows the creep strain rate ($\dot{\varepsilon}$) of AD sample calculated from the fits of creep displacement–time curves during creep deformation. The creep strain rate increases slightly with loading rate increasing. Furthermore, the creep strain rate decreases rapidly at transient creep stage and subsequently reaches a nearly constant value on the order of 10^{-4} at the steady-state stage. It has been reported that the creep strain rate in steady-state stage can be considered as a dynamic equilibrium between free volume formation, which results in plastic flow softening and annihilation which contributes to hardening [29]. In addition, free volume formation results in a much more homogeneous creep deformation at higher strain rates, which explains the high sensitivity of the creep stress to the loading rate, as shown in Fig. 7a. The derived creep strain rates as a function of the holding time are shown in Fig. 7d. The creep strain rate increases with the number of CTC cycles, especially for sample CTC15. Thus, CTC treatment increases the transition time from primary-state stage to steady-state stage.

3.3 Effects of CTC treatment on optical properties

The effect of microstructural changes after different numbers of CTC cycles on optical properties of MGTFs remains an unresolved mystery. Optical parameters such as refractive index (n) and extinction coefficient (k) are key parameters for characterizing optical performance of MGTFs. Specifically, n is a key parameter that reflects light dispersion properties, and k is an important indicator of light wave decay. Therefore, both refractive index n and extinction coefficient k were measured as functions of the

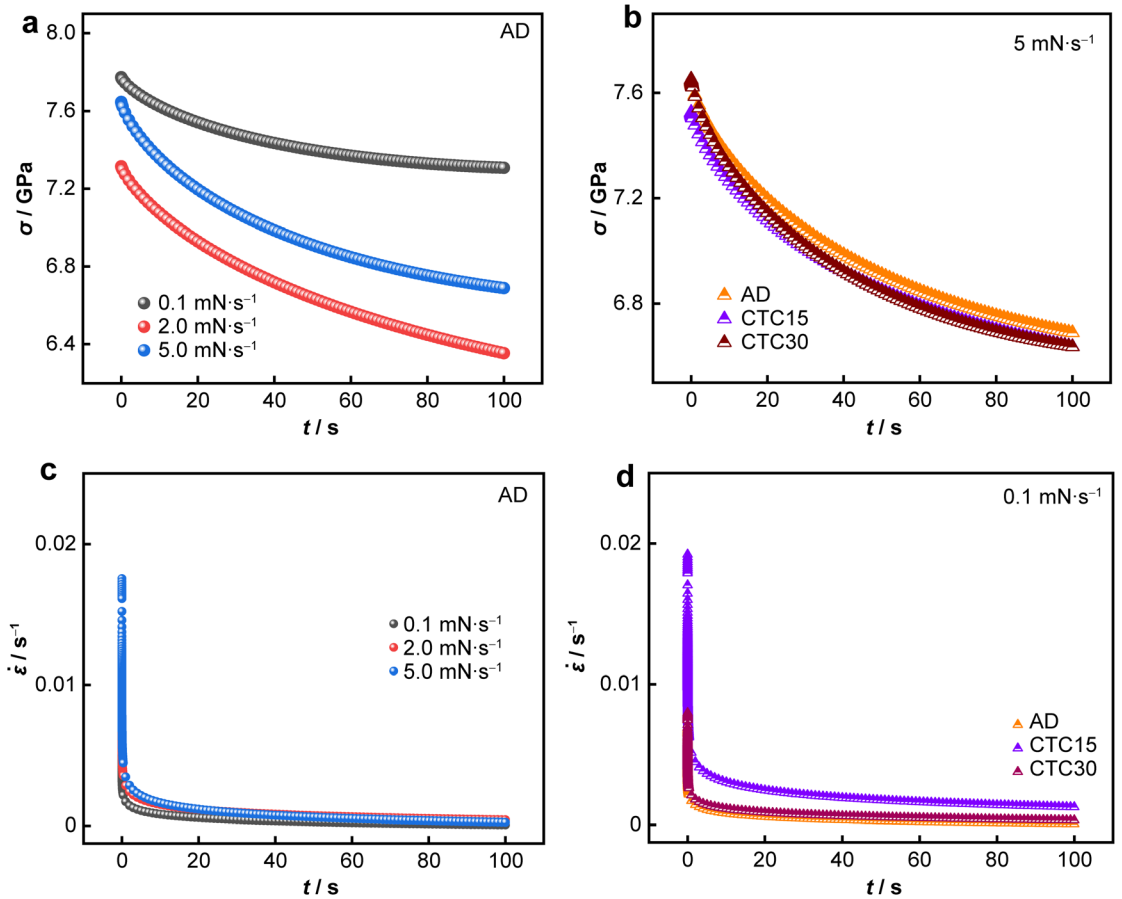

Fig. 7 **a** Creep stress (σ) versus holding time (t) under different loading rates; **b** creep stress under loading rate of 5 $mN{\cdot}s^{-1}$; **c** creep strain rate ($\dot{\varepsilon}$) as a function of loading rates; **d** creep strain rate during holding stage under loading rate of 0.1 $mN{\cdot}s^{-1}$

wavelength λ in the visible spectrum from 350 to 500 nm (Fig. 8a, b). Within the visible wavelength range, n for each sample assumes an almost constant value regardless of the wavelength. However, k is significantly affected by λ. For the three samples, k decreases from 2.63 to 0.21 as λ increases. As λ increases further, k decreases slightly from 0.21 to 0.13. The values of n and k are comparable to those of nano-patterned Pt-MGs, which have the disadvantage of containing noble elements [33]. Both n and k depend on the density and structural heterogeneity. Their variation upon CTC treatment is discussed later.

The reflectivity (R) is another indicator of optical performance. The theoretical reflectivity R_t can be expressed as [5]:

$$R_t = 1 - \frac{4n}{(1+n)^2+k^2} \tag{6}$$

As λ increases, an evident decrease in R_t can be observed, as shown in Fig. 8c. To verify the validity of the calculated R_t based on n and k, experimental R values of MGTFs before and after CTC were measured at λ between 380 and 1000 nm and the results are shown in Fig. 8d. Comparing the results for λ shorter than 500 nm, it can be seen that R and R_t have nearly the same values, which indicates that the experimental results are in good agreement with theoretical prediction from Eq. (6). The R of sample CTC15 is significantly higher than those of the other two samples. In general, a larger k causes faster decay of the light amplitude within the film and a lower intensity of the light entering the film. This increases the reflected light and results in a higher R [5].

4 Discussion

Carefully structural observations were performed to understand the effects of CTC on the mechanical heterogeneity. As shown in Fig. 9a–c, amorphous nature is corroborated by the maze-like features in HRTEM images and the diffuse halo rings of selected area electron diffraction (SAED) patterns [34, 35]. It has been reported that CTC treatment has an important influence on nanoscale structures by affecting local crystal-like ordering (CLO) fraction [36]. An autocorrelation analysis was therefore carried out

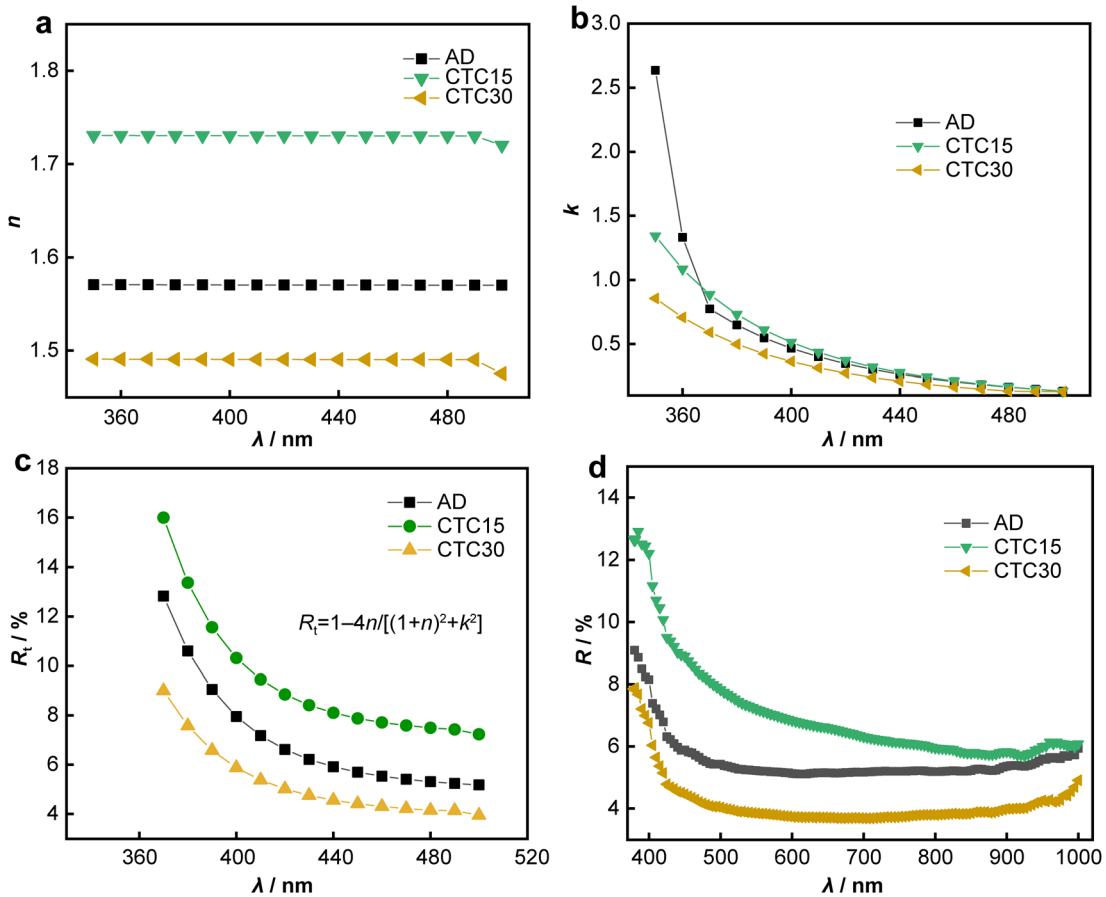

Fig. 8 Optical parameters: **a** refractive index (n), **b** extinction coefficient (k), **c** theoretical reflectivity (R_t) and **d** experimental reflectivity (R) of AD, CTC15 and CTC30 samples within visible light wavelength range

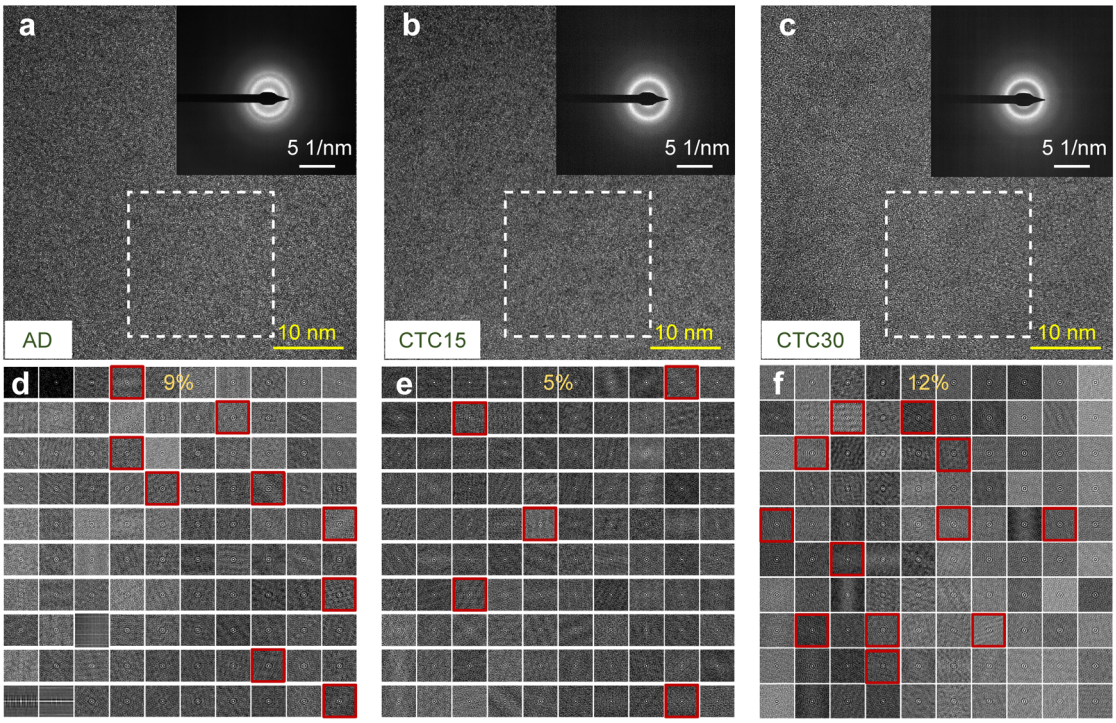

Fig. 9 HRTEM images and corresponding analysis: HRTEM images and (insets) corresponding SAED patterns of samples **a** AD, **b** CTC15, and **c** CTC30; **d–f** 2D autocorrelation function analysis results of randomly selected squares in **a–c**, respectively

to quantitatively analyse structural ordering of the three samples and resultant images are shown in Fig. 9d–f. The sub-images with clear atomic fringe features are considered as ordered and highlighted by red rectangles. Pattern in the first row and the fourth column in Fig. 9d is taken as the reference figure. If the stripe pattern is more obvious than it, it is identified as CLO structure. Total fractions of CLO structures are 9% in the AD sample, 5% in the CTC15 sample, and 12% in the CTC30 sample. This result indicates that some of CLO structures are destroyed after 15 CTC cycles, whereas further cycling facilitates the formation of an ordered structure [37]. It has also been reported that a lower cycling temperature destroyed part of CLO structure whereas a higher cycling temperature facilitated the formation of an ordered structure in FeCoBSiNb and FeCoBSiNbCu MGs [27, 37]. Local structures with CLO have been widely observed in Zr-based MGs and may act as fertile sites for β-relaxation and STZ activation [38]. It is worth noting that CTC can lead to rejuvenation, relaxation and oscillatory (rejuvenation-relaxation transition) behaviours [39, 40]. Molecular dynamics simulations have also shown that CTC treatment can induce BMG rejuvenation and relaxation depending on the nature of bonding and initial structural homogeneities [30, 41]. Typically, rejuvenation plays a dominant role at a smaller cycling number, whereas relaxation becomes more crucial as cycling number increases [42]. Thus, the variation in CLO structure fraction can be attributed to the competition between relaxation and rejuvenation due to CTC treatment and indicates a change in the distribution between short to medium-range orders [43–45]. Relaxation-rejuvenation competition has already been verified by the increase-then-decrease variation in mechanical heterogeneity (as seen from modulus and energy dissipation distributions) [46]. These results indicate that CLO fraction is sensitive to the number of CTC cycles and that a more inhomogeneous atomic configuration can be achieved in MGTFs with an appropriate number of cycles. The mechanical properties of nanostructured MGTFs are therefore altered by their structural heterogeneity.

High-angle annual dark-field scanning TEM (HAADF-STEM) observations were conducted to further evaluate the effect of CTC on spatial heterogeneities and to understand atomic mechanism of creep deformation in Zr-based MGTFs. Heterogeneous contrast with alternating dark and bright domains at nanometer scale is clearly observed in Fig. 10a–c. A core–shell model has been proposed to characterize the nanoscale heterogeneity of MGs [47]. The bright regions in HAADF images have a relatively high density, which corresponds to solid-like regions [48, 49]. In contrast, the dark regions have a lower density, which corresponds to liquid-like regions. Heterogeneous MGTFs with different sites have different coefficients of thermal expansion (CTE); therefore, applying CTC can induce non-affine atomic deformation,

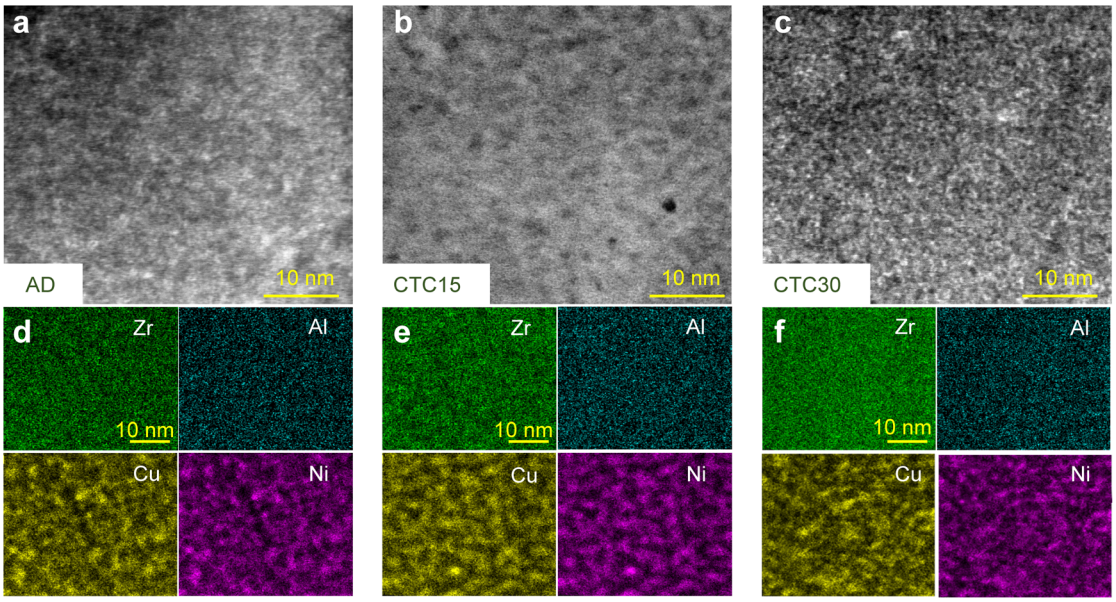

Fig. 10 **a–c** HAADF-TEM images and **d–f** corresponding elemental mappings of samples AD, CTC15 and CTC30

which leads to changes in heterogeneity [39, 50]. As shown in Fig. 10b, HAADF-STEM image of CTC15 sample shows the strongest contrast and apparent dark regions with sizes of ~2–3 nm, which further confirms that it is the structure with the highest heterogeneity. This coincides with the occurrence of the widest hardness, modulus and energy dissipation distributions in CTC15, which indicates rejuvenation. The CTC30 sample has the most homogenous structure, as shown in Fig. 10c, which implies that the relaxation process has the dominant effect on atomic arrangement.

Based on the above analysis, the enhancement in peak intensity and the shift of the peaks to longer relaxation time can be attributed to their increased structural heterogeneity [51]. The conspicuous second relaxation peak in CTC15 indicates the existence of loosely arranged regions. Upon further increasing the number of CTC cycles, the relaxation spectrum of MGTFs shifts to a shorter relaxation time, indicating an acceleration of the two relaxation processes [52]. For the relaxation process with shorter relaxation time (the first relaxation peak), the relaxation intensity does not change significantly when the number of CTC cycles is increased from 15 to 30. This is attributed to the production of more weakly bonded regions by internal stress introduced by CTC, which promotes atomic motion when CTC cycles is lower than a certain threshold. The internal stress due to cooling contraction during CTC activates atomic motion in soft regions and results in short-range ordering (SRO) via the mobile atoms [52]. The increase in free volume also facilitates the activation of defects in soft regions. However, when CTC cycles exceed a certain value, the increased atomic packing hinders atomic flow in the weakly bonded regions of the total glassy structure [51]. However, the detailed atomic mechanism of nanoscale creep deformation requires further investigation.

The optical properties of nanostructured MGTFs are correlated with their surface roughness and structural heterogeneity. In this study, because the RMS roughness of Zr-based MGTFs before and after CTC is almost the same (1.5 nm), the variation in their optical parameters originates mainly from the change in structural heterogeneity. In particular, the population of liquid-like regions (dark) in Fig. 10b, which have lower elastic stiffness and higher CTE, initially increases and then decreases with increasing CTC cycles. When MGTFs are treated with more CTC cycles, the cooling contraction introduces thermal stress and facilitates the coalescence of soft spots/domains, leading to free volume annihilation and homogeneity [39]. In addition, elemental mappings (Fig. 10d–f) show homogeneous distributions of Zr and Al in all alloys, while the intense yellow and purple regions indicate high local concentrations of Cu and Ni elements. The differences in the elemental distribution can be attributed to the rapid diffusion of elements as a result of their different CTEs and temperature increase during CTC [38]. Based on the above analysis, the pronounced enhancement of R in CTC15 sample can be attributed to the increased chemical heterogeneities due to changes in atomic-level stress distribution induced by CTC.

5 Conclusion

In summary, nanostructured $Zr_{64.13}Cu_{15.75}Ni_{10.12}Al_{10}$ MGTFs were produced by keeping T_{sub} at room

temperature (0.41 T_{sub} for Zr-based MGTFs) and a low deposition rate of 3.97 nm·min^{-1} using magnetron sputtering. Influence of CTC on mechanical and structural heterogeneity, nanoscale creep deformation and optical characteristics was systematically investigated. The initial increase and subsequent decrease in mechanical heterogeneity of Zr-based MGTFs with increasing CTC cycles indicate competition between the relaxation and rejuvenation processes. The creep displacement during constant load-holding period is well described by Maxwell–Voigt model with two Kelvin units. Relaxation time spectra results imply that more defects with larger-sized soft regions are preferentially activated in CTC-treated samples. CTC treatment increases the transition time from the primary-state stage to the steady-state stage during creep deformation. Refractive index remains almost unchanged at different CTC cycles regardless of the wavelength. However, the extinction coefficient and reflectivity show a negative correlation with the wavelength. Moreover, the experimental data for the reflectivity is in good agreement with the calculated values. The enhanced R after appropriate CTC cycles mainly arises from the increased local aggregation of Cu and Ni elements at several nanometers.

These results therefore provide new insights into the relationship between spatial heterogeneity, nanoscale creep deformation and optical properties of MGs. These insights can guide the development of novel nanostructured MGTFs with enhanced functional performance for important engineering applications in solar heaters, optical coatings and microelectromechanical devices.

Acknowledgements This study was financially supported by the National Natural Science Foundation of China (Nos. 51971061 and 52231005) and the Natural Science Foundation of Jiangsu Province (No. BK20221474).

Declarations

Conflict of interests The authors declare that they have no conflict of interests.

References

[1] Song L, Gao M, Xu W, Huo J, Wang J, Li R, Wang W, Perepezko JH. Inheritance from glass to liquid: β relaxation depresses the nucleation of crystals. Acta Mater. 2020;185:38. https://doi.org/10.1016/j.actamat.2019.12.002.

[2] Zhang P, Maldonis JJ, Liu Z, Schroers J, Voyles PM. Spatially heterogeneous dynamics in a metallic glass forming liquid imaged by electron correlation microscopy. Nat Commun. 2018;9(1):1129. https://doi.org/10.1038/s41467-018-03604-2.

[3] Yuan C, Lv Z, Pang C, Li X, Liu R, Yang C, Ma J, Ke H, Wang W, Shen B. Ultrasonic-assisted plastic flow in a Zr-based metallic glass. Sci China Mater. 2020;64(2):448. https://doi.org/10.1007/s40843-020-1411-2.

[4] Lv Z, Yuan C, Ke H, Shen B. Defects activation in CoFe-based metallic glasses during creep deformation. J Mater Sci Technol. 2021;69:42. https://doi.org/10.1016/j.jmst.2020.08.012.

[5] Yao W, Cao Q, Liu S, Wang X, Fecht HJ, Caron A, Zhang D, Jiang J. Tailoring nanostructured Ni-Nb metallic glassy thin films by substrate temperature. Acta Mater. 2020;194:13. https://doi.org/10.1016/j.actamat.2020.04.046.

[6] Wang Y, Ding J, Fan Z, Tian L, Li M, Lu H, Zhang Y, Ma E, Li J, Shan Z. Tension-compression asymmetry in amorphous silicon. Nat mater. 2021;20:1371. https://doi.org/10.1038/s41563-021-01017-z.

[7] Ghidelli M, Gravier S, Blandin JJ, Raskin JP, Lani F, Pardoen T. Size-dependent failure mechanisms in ZrNi thin metallic glass films. Scripta Mater. 2014;89:9. https://doi.org/10.1016/j.scriptamat.2014.06.011.

[8] Lee CJ, Lin HK, Sun S, Huang J. Characteristic difference between ITO/ZrCu and ITO/Ag bi-layer films as transparent electrodes deposited on PET substrate. Appl Surf Sci. 2010;257(1):239. https://doi.org/10.1016/j.apsusc.2010.06.074.

[9] Alvi S, Milczarek M, Jarzabek DM, Hedman D, Kohan MG, Levintant-Zayonts N, Vomiero A, Akhtar F. Enhanced mechanical, thermal and electrical properties of high-entropy HfMoNbTaTiVWZr thin film metallic glass and its nitrides. Adv Eng Mater. 2022. https://doi.org/10.1002/ADEM.202101626.

[10] Liu S, Cao Q, Qian X, Wang C, Wang X, Zhang D, Hu X, Xu W, Ferry M, Jiang J. Effects of substrate temperature on structure, thermal stability and mechanical property of a Zr-based metallic glass thin film. Thin Solid Films. 2015;595:17. https://doi.org/10.1016/j.tsf.2015.10.049.

[11] Pei C, Chen S, Zhao T, Li M, Cui Z, Sun B, Hu S, Lan S, Hahn H, Feng T. Nanostructured metallic glass in a highly upgraded energy state contributing to efficient catalytic performance. Adv mater. 2022;34(26):2200850. https://doi.org/10.1002/adma.202200850.

[12] Sun Q, Miskovic DM, Ferry M. Probing the formation of ultrastable metallic glass from structural heterogeneity. J Mater Sci Technol. 2022;104:214. https://doi.org/10.1016/J.JMST.2021.06.059.

[13] Luo P, Cao C, Zhu F, Lv Y, Liu Y, Wen P, Bai H, Vaughan G, Michiel M, Ruta B, Wang W. Ultrastable metallic glasses formed on cold substrates. Nat commun. 2018;9(1):1389. https://doi.org/10.1038/s41467-018-03656-4.

[14] Sun Q, Miskovic DM, Kong H, Ferry M. Transition from relaxation to rejuvenation in ultrastable metallic glass driven by annealing. Appl Surf Sci. 2021;546:149048. https://doi.org/10.1016/j.apsusc.2021.149048.

[15] Luo Q, Zhang Z, Li D, Luo P, Wang W, Shen B. Nanoscale--to-Mesoscale heterogeneity and percolating favored clusters govern ultrastability of metallic glasses. Nano lett. 2022;22:2867. https://doi.org/10.1021/ACS.NANOLETT.1C05039.

[16] Nandam SH, Ivanisenko Y, Schwaiger R, Śniadecki Z, Mu X, Wang D, Chellali R, Boll T, Kilmametov A, Bergfeldt T, Gleiter H, Hahn H. Cu-Zr nanoglasses: atomic structure, thermal stability and indentation properties. Acta Mater. 2017;136:181. https://doi.org/10.1016/j.actamat.2017.07.001.

[17] Wang J, Chen N, Liu P, Wang Z. The ultrastable kinetic behavior of an Au-based nanoglass. Acta Mater. 2014;79:30. https://doi.org/10.1016/j.actamat.2014.07.015.

[18] Gleiter H, Schimmel T, Hahn H. Nanostructured solids–from nano-glasses to quantum transistors. Nano Today. 2014;9(1):17. https://doi.org/10.1016/j.nantod.2014.02.008.

[19] Gleiter H. Nanoglasses: a new kind of noncrystalline material and the way to an age of new technologies? Small. 2016;12(16):2225. https://doi.org/10.1002/smll.201500899.

[20] Liu Y, Zhao F, Li Y, Chen M. Deformation behavior of metallic glass thin films. J Appl Phys. 2012;112(6):063504. https://doi.org/10.1063/1.4752280.
[21] Yuan C, Liu R, Pang C, Zuo X, Li B, Song S, Hu J, Zhu W, Shen B. Anelastic and viscoplastic deformation in a Fe-based metallic glass. J Alloys Compd. 2021;853:157233. https://doi.org/10.1016/j.jallcom.2020.157233.
[22] Trifonov AS, Lubenchenko AV, Louzguine-Luzgin DV. Cryogenic cycling-induced changes in a Fe-based bulk metallic glass on the nanoscale surface layer. Mater Lett. 2021;285:129114. https://doi.org/10.1016/j.matlet.2020.129114.
[23] Widjaja G, Ershov K, Chupradit S, Suksatan W, Kavitha M, Jawad MA, Fardeeva I, Ghafel ST, Mustafa YF, Kadhim MM, Sajjadifar S. The effects of hydrogen doping on energy state of shear bands in a Zr-based metallic glass. Vacuum. 2022;198:110882. https://doi.org/10.1016/j.vacuum.2022.110882.
[24] Ross P, Küchemann S, Derlet PM, Yu H, Arnold W, Liaw P, Samwer K, Maaß R. Linking macroscopic rejuvenation to nano-elastic fluctuations in a metallic glass. Acta Mater. 2017;138:111. https://doi.org/10.1016/j.actamat.2017.07.043.
[25] Wang D, Liu Y, Nishi T, Nakajima K. Length scale of mechanical heterogeneity in a glassy polymer determined by atomic force microscopy. Appl Phys Lett. 2012;100(25):251905. https://doi.org/10.1063/1.4729931.
[26] Yuan C, Lv Z, Pang C, Zhu W, Wang X, Shen B. Pronounced nanoindentation creep deformation in Cu-doped CoFe-based metallic glasses. J Alloys Compd. 2019;806:246. https://doi.org/10.1016/j.jallcom.2019.07.226.
[27] Di S, Ke H, Wang Q, Zhou J, Zhao Y, Shen B. Large tensile plasticity induced by pronounced β-relaxation in Fe-based metallic glass via cryogenic thermal cycling. Mater Design. 2022;222:111074. https://doi.org/10.1016/J.MATDES.2022.111074.
[28] Guo H, Jiang C, Yang B, Wang J. Deformation behavior of Al-rich metallic glasses under nanoindentation. J Mater Sci Technol. 2017;33(11):1272. https://doi.org/10.1016/j.jmst.2016.10.014.
[29] Liu S, Chang Z, Fu Y, Liu Y, Lin M, Ren X, Wang W, Zhang Z, He J. Nanoscale creep behavior and its size dependency of a Zr-based bulk metallic glass manufactured by selective laser melting. Mater Design. 2022;218:110723. https://doi.org/10.1016/J.MATDES.2022.110723.
[30] Shang B, Wang W, Greer AL, Guan P. Atomistic modelling of thermal-cycling rejuvenation in metallic glasses. Acta Mater. 2021;213:116952. https://doi.org/10.2139/ssrn.3757770.
[31] Liu Y, Wang D, Nakajima K, Zhang W, Hirata A, Nishi T, Inoue A, Chen M. Characterization of nanoscale mechanical heterogeneity in a metallic glass by dynamic force microscopy. Phys Rev Lett. 2011;106(12):125504. https://doi.org/10.1103/PhysRevLett.106.125504.
[32] Castellero A, Moser B, Uhlenhaut DI, Torre FHD, Löffler JF. Room-temperature creep and structural relaxation of Mg–Cu–Y metallic glasses. Acta Mater. 2008;56(15):3777. https://doi.org/10.1016/j.actamat.2008.04.021.
[33] Hendra J, Tarigan NK, Ramos N, Golden K, Ayrton AB. Low reflectance of nano-patterned Pt-Cu-NiP bulk metallic glass. Appl Phys Lett. 2015;107(2):021903. https://doi.org/10.1063/1.4926873.
[34] Ying H, Liu S, Wu Z, Dong W, Ge J, Hahn H, Provenzano V, Wang X, Lan S. Phase selection rule of high-entropy metallic glasses with different short-to-medium-range orders. Rare Met. 2022;41(6):2021. https://doi.org/10.1007/s12598-022-01973-8.
[35] Li K, Ge J, Liu S, Fu S, Yin Z, Zhang W, Chen G, Wei S, Ji H, Feng T, Liu Q, Wang X, Zuo X, Ren Y, Hahn H, Lan S. In situ scattering study of multiscale structural evolution during liquid–liquid phase transition in Mg-based metallic glasses. Rare Met. 2021;40(11):3107. https://doi.org/10.1007/s12598-021-01767-4.
[36] Di S, Wang Q, Zhou J, Shen Y, Li J, Zhu M, Yin K, Zeng Q, Sun L, Shen B. Enhancement of plasticity for FeCoBSiNb bulk metallic glass with superhigh strength through cryogenic thermal cycling. Scripta Mater. 2020;187:13. https://doi.org/10.1016/j.scriptamat.2020.05.059.
[37] Di S, Wang Q, Yang Y, Liang T, Zhou J, Su L, Yin K, Zeng Q, Sun L, Shen B. Efficient rejuvenation of heterogeneous $\{[(Fe_{0.5}Co_{0.5})_{0.75}B_{0.2}Si_{0.05}]_{96}Nb4\}_{99.9}Cu_{0.1}$bulk metallic glass upon cryogenic cycling treatment. J Mater Sci Technol. 2022. https://doi.org/10.1016/j.jmst.2021.04.034.
[38] Geng C, Huang B, Zhang N, Yi J, Wang Q, Jia Y, Li F, Luan J, Hou X, Huang W, Yuan Q, Wang G, Wang W. Evolution of local densities during shear banding in Zr-based metallic glass micropillars. Acta Mater. 2022;235:118068. https://doi.org/10.2139/ssrn.4013247.
[39] Sohrabi S, Ri M, Jiang H, Gu L, Wen P, Sun Y, Wang W. Prominent role of chemical heterogeneity on cryogenic rejuvenation and thermomechanical properties of La–Al–Ni metallic glass. Intermetallics. 2019;111:106497. https://doi.org/10.1016/j.intermet.2019.106497.
[40] Gu J, Shao Y, Shi L, Si J, Yao K. Novel corrosion behaviours of the annealing and cryogenic thermal cycling treated Ti-based metallic glasses. Intermetallics. 2019;110:106467. https://doi.org/10.1016/j.intermet.2019.04.010.
[41] Ketov SV, Trifonov AS, Ivanov YP, Churyumov AY, Lubenchenko AV, Batrakov AA, Jiang J, Louzguine LD, Eckert J, Orava J, Greer AL. On cryothermal cycling as a method for inducing structural changes in metallic glasses. NPG Asia Mater. 2018;10(4):137. https://doi.org/10.1038/s41427-018-0019-4.
[42] Tang Y, Xiao H, Wang X, Cao Q, Zhang D, Jiang J. Mechanical property and structural changes by thermal cycling in phase-separated metallic glasses. J Mater Sci Technol. 2021;78:144. https://doi.org/10.1016/j.jmst.2020.10.050.
[43] Lan S, Zhu L, Wu Z, Gu L, Zhang Q, Kong H, Liu J, Song R, Liu S, Sha G, Wang Y, Liu Q, Liu W, Wang P, Liu C, Ren Y, Wang X. A medium-range structure motif linking amorphous and crystalline states. Nat mater. 2021;20(10):1347. https://doi.org/10.1038/s41563-021-01011-5.
[44] Lan S, Ren Y, Wei X, Wang B, Gilbert EP, Shibayama T, Watanabe S, Ohnuma M, Wang X. Hidden amorphous phase and reentrant supercooled liquid in Pd-Ni-P metallic glasses. Nat Commun. 2017;8:14679. https://doi.org/10.1038/ncomms14679.
[45] Lan S, Guo C, Zhou W, Ren Y, Almer J, Pei C, Hahn H, Liu C, Feng T, Wang X, Gleiter H. Engineering medium-range order and polyamorphism in a nanostructured amorphous alloy. Commun Phys. 2019;2:117. https://doi.org/10.1038/s42005-019-0222-9.
[46] Cui J, Luo Q, Di S, Zhang Z, Shen B. Rejuvenation-to-relaxation transition induced by elastostatic compression and its effect on deformation behavior in a Zr-based bulk metallic glass. Metals. 2022;12(2):282. https://doi.org/10.3390/MET12020282.
[47] Ke H, Zeng J, Liu C, Yang Y. Structure heterogeneity in metallic glass: modeling and experiment. J Mater Sci Technol. 2014;30(6):560. https://doi.org/10.1016/j.jmst.2013.11.014.
[48] Luo P, Zhu F, Lv Y, Lu Z, Shen L, Zhao R, Sun Y, Vaughan GBM, Michiel M, Ruta B, Bai H, Wang W. Microscopic structural evolution during ultrastable metallic glass formation. ACS Appl Mater Interfaces. 2021;13:40098. https://doi.org/10.1021/acsami.1c10716.
[49] Zhu F, Hirata A, Liu P, Song S, Tian Y, Han J, Fujita T, Chen M. Correlation between local structure order and spatial heterogeneity in a metallic glass. Phys Rev Lett. 2017;119(21):215501. https://doi.org/10.1103/PhysRevLett.119.215501.

[50] Ketov SV, Sun Y, Nachum S, Lu Z, Checchi A, Beraldin AR, Bai H, Wang W. Rejuvenation of metallic glasses by non-affine thermal strain. Nature. 2015;524(7564):200. https://doi.org/10.1038/nature14674.

[51] Zhu Y, Zhou Y, Wang A, Li H, Fu H, Zhang H, Zhang H, Zhu Z. Atomic-scale icosahedral short-range ordering in a rejuvenated Zr-based bulk metallic glass upon deep cryogenic treatment. Mater Sci Eng-A. 2022;850:143565. https://doi.org/10.1016/j.msea.2022.143565.

[52] Ma X, Ma J, Bian X, Tong X, Han D, Jia Y, Wu S, Zhang N, Geng C, Li P, Wang Q, Zhang Y, Wang G. The role of nano-scale elastic heterogeneity in mechanical and tribological behaviors of a Cu–Zr based metallic glass thin film. Intermetallics. 2021;133:107159. https://doi.org/10.1016/j.intermet.2021.107159.